The Effect of Inhomogeneous Compression on Water Transport in the Cathode of a Proton Exchange Membrane Fuel Cell

Anders C. Olesen[1]
e-mail: aco@et.aau.dk

Torsten Berning
e-mail: tbe@et.aau.dk

Søren K. Kær
e-mail: skk@et.aau.dk

Department of Energy Technology,
Aalborg University,
Aalborg East, 9220 Denmark

A three-dimensional, multicomponent, two-fluid model developed in the commercial CFD package CFX 13 (ANSYS Inc.) is used to investigate the effect of porous media compression on water transport in a proton exchange membrane fuel cell (PEMFC). The PEMFC model only consist of the cathode channel, gas diffusion layer, microporous layer, and catalyst layer, excluding the membrane and anode. In the porous media liquid water transport is described by the capillary pressure gradient, momentum loss via the Darcy-Forchheimer equation, and mass transfer between phases by a nonequilibrium phase change model. Furthermore, the presence of irreducible liquid water is taken into account. In order to account for compression, porous media morphology variations are specified based on the gas diffusion layer (GDL) through-plane strain and intrusion which are stated as a function of compression. These morphology variations affect gas and liquid water transport, and hence liquid water distribution and the risk of blocking active sites. Hence, water transport is studied under GDL compression in order to investigate the qualitative effects. Two simulation cases are compared; one with and one without compression. [DOI: 10.1115/1.4006475]

1 Introduction

To evolve the area of PEM fuel cell (PEMFC) and bring it to a commercial level, a better understanding of basic interactions is needed to improve PEMFC durability and operation. A generic problem in PEMFC is water management, which affects both the cell performance and degradation. Too little water dries out the FC electrolyte membrane and hinders proton conduction; whereas too much water hinders transport of oxygen and fuel. While many studies on water transport and water management assume homogeneous gas diffusion layer (GDL) properties [1–5], a heterogeneous structure is typically seen due to compression. Under the land the GDL is fairly uniformly compressed but at the channel compression is nonuniform due to GDL intrusion. As a consequence mass transport increases towards the middle of the channel caused by a higher porosity and permeability.

A general review of GDL properties and the effect of compression on these can be found in Ref. [6]. A few recent modeling efforts are highlighted in the following.

Hottinen et al. [7] studied mass and charge transfer under inhomogeneous compression. Experimentally evaluated GDL properties such as porosity, permeability, and contact resistance were correlated to the GDL thickness. Based on these properties it was found via a single-phase, two-dimensional model that inhomogeneous compression significantly effects lifetime and local performance. Later, Nitta et al. [8] carried out a new study on inhomogeneous compression based on the same material data as [7]. This time, a more advanced transport model was used in addition to a new equation for the intrusion, but still neglecting multiphase phenomena. They showed that the inhomogeneous compression caused a lower local current density under the channel then under the land; in contrast to earlier studies. Furthermore, it was emphasized that the model did not take phase change and liquid water transport into account, which could significantly affect transport phenomena and performance.

A different approach to modeling compression effects on GDL properties was chosen in Ref. [9]. A finite element model (FEM) of the GDL was coupled with a two-dimensional, two-phase model of a PEMFC. The FEM model determined the intrusion, porosity distribution, and ohmic contact resistance as function of compression. Based on the porosity, such properties as the permeability and tortuosity were estimated via empirical correlations. Their results showed that performance decreased with increasing compression, and that an optimal compression exists if contact resistance is considered.

Based on the literature review it can be concluded that no comprehensive three-dimensional, nonisothermal, two-phase flow model has been used to investigate the effect of inhomogeneous compression on the cathode water transport. Important phenomena such as liquid water transport and phase change have often been neglected in the literature. Therefore, including these phenomena can give a more physically sound picture.

The primary objective of this research effort is to develop a model for studying the effect of intrusion and inhomogeneous GDL properties on water management.

In this paper a novel inhomogeneous compression model based on intrusion and strain measurements is coupled with a three-dimensional, two-phase flow, multicomponent, and nonisothermal half-cell model of a PEMFC. In order to test the model a simulation case with and another without compression is depicted and discussed.

2 Model Description

The newly developed three-dimensional, steady-state, multiphase flow, multicomponent, and nonisothermal PEMFC model currently considers the cathode side only. The PEMFC model was developed in the commercial CFD software ANSYS CFX 13. The two-phase flow model employed is based on the multifluid approach, i.e., the model solves for one set of transport equations for each phase. The multifluid approach uses the notion of interpenetrating continua, and hence inherently only captures statistical macroscopic phenomenon. In the channel two phases are

[1]Corresponding author.

Contributed by the Advanced Energy Systems Division of ASME for publication in the Journal of Fuel Cell Science and Technology. Manuscript received December 9, 2011; final manuscript received March 6, 2012; published online April 26, 2012. Editor: Nigel M. Sammes.

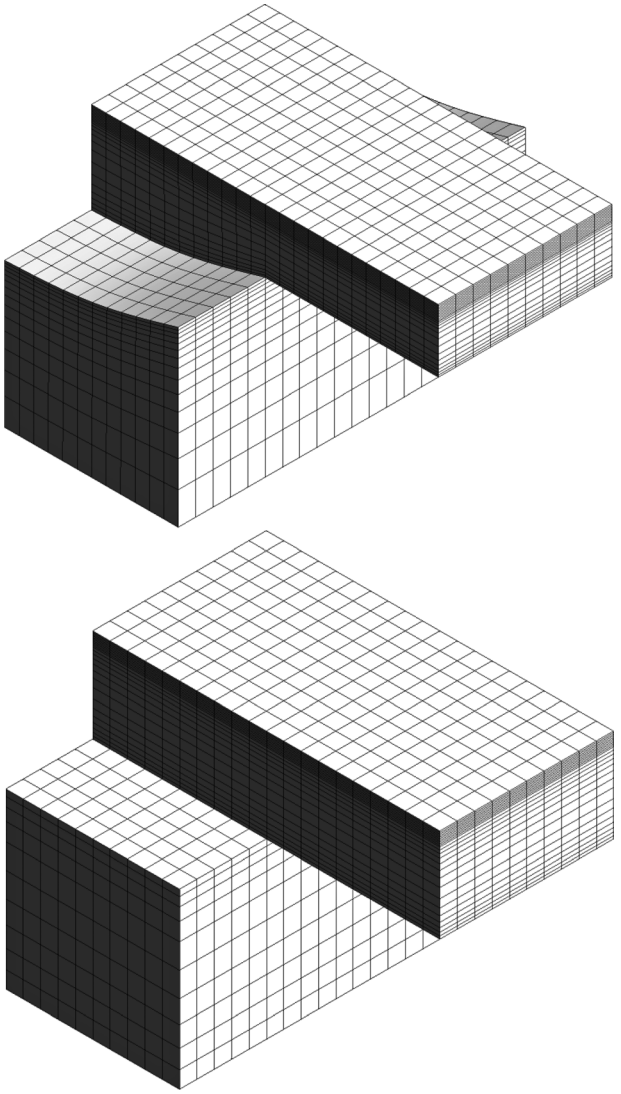

Fig. 1 Computational domain with and without compression

assumed present: liquid and gas. In the porous media an additional solid phase is present. Hence, heat transfer in all three phases is included in the model.

2.1 Model Geometry. The geometries used in the study are depicted in Fig. 1. Each mesh comprises approximately 13,000 hexahedral elements. The computational domain consists of a gas flow channel with attached porous media (GDL, micro porous layer (MPL), and catalyst layer (CL)). The bipolar plates (BPs) are currently neglected. The initial thickness of the GDL, MPL, and CL are 230, 20, and 20 μm, respectively. Furthermore, the channel width and height along with land width is 1, 0.5, and 1 mm, respectively.

2.2 Assumptions. In order to simplify modeling the following assumptions were made:

- Instead of a cooling channel a constant temperature boundary is specified at the GDL/BP and channel/BP interface.
- It is assumed that no heat or mass is transported through the membrane.
- The oxygen reduction reaction (ORR) at the cathode is assumed to produce liquid water.
- A constant overvoltage is assumed in the reaction rate equation since the PEMFC model does not solve for proton or electron transport.
- The gas phase consists of nitrogen, oxygen, and water (i.e., N_2, O_2 and $H_2O_{(g)}$). Whereas the liquid phase only comprises of liquid water ($H_2O_{(l)}$).
- Gases are assumed to be ideal.
- All phases share the same pressure field.
- In the case of inhomogeneous compression it is assumed that the CL and MPL thickness does not change. A similar assumption was made in [8].
- The change in thermal contact resistance with compression is not accounted for.

2.3 Governing Equations. The complete set of conservation equation, which are solved for each fluid phase in order to obtain the flow field, component concentration, and temperature, are depicted in Eqs. (1)–(4).

Continuity equation:

$$\nabla \cdot \varepsilon s_\alpha \rho_\alpha \mathbf{U}_\alpha = \varepsilon s_\alpha \mathbf{S}_\alpha + (\dot{m}_{\alpha\beta} - \dot{m}_{\beta\alpha}) \tag{1}$$

where α denotes the phase, and $\dot{m}_{\alpha\beta}$ and $\dot{m}_{\beta\alpha}$ are the directionally dependent interfacial mass flows.

Momentum equation:

$$\nabla \cdot \varepsilon s_\alpha(\rho_\alpha \mathbf{U}_\alpha \mathbf{U}_\alpha - \nabla \cdot \tau) = \varepsilon s_\alpha(\mathbf{S}_\alpha - \nabla p_\alpha) + \varepsilon \mathbf{M}_\alpha + (\dot{m}_{\alpha\beta}\mathbf{U}_\beta - \dot{m}_{\beta\alpha}\mathbf{U}_\alpha) \tag{2}$$

where τ is the stress tensor and $\mathbf{M}_\alpha$ are the interfacial forces acting on phase α due to the presence of other phases.

Energy equation:

$$\nabla \cdot \varepsilon s_\alpha(\rho_\alpha U_\alpha H_\alpha - \lambda_\alpha \nabla T_\alpha) = \varepsilon s_\alpha \mathrm{S}_\alpha + \nabla \cdot \varepsilon s_\alpha \sum_{i=1}^{N_c} \Gamma_i h_i \nabla Y_i + (\dot{m}_{\alpha\beta} H_\beta - \dot{m}_{\beta\alpha} H_\alpha) \tag{3}$$

where H is the static enthalpy and N_C is the number of species. The energy equation is simplified by neglecting kinetic energy. This simplification is justified because the flow in microporous channels involve low flow speeds.

Species equation:

$$\nabla \cdot \varepsilon s_\alpha(\rho_\alpha \mathbf{U}_\alpha Y_{A\alpha} - \rho_\alpha D_{A\alpha} \nabla Y_{A\alpha}) = \varepsilon s_\alpha \mathrm{S}_\alpha + (\dot{m}_{\alpha\beta} Y_{A\beta} - \dot{m}_{\beta\alpha} \mathrm{Y}_{A\alpha}) \tag{4}$$

where $Y_{A\alpha}$ denotes mass fraction of component A in phase α.

2.4 Source Terms. In order to model the reaction rate/current density resulting from the electrochemical reaction at the cathode, the Butler-Volmer equation is used [10]:

$$j = j_0^T \left[\exp\left(\frac{\alpha F}{RT}\eta_c\right) - \exp\left(\frac{-(1-\alpha)F}{RT}\eta_c\right)\right] \tag{5}$$

$$j_0^T = (1-s) a j_0^{T_0} \left(\frac{\xi Co_2}{Co_{2,\mathrm{ref}}}\right) \exp\left[\frac{-E_{\mathrm{act}}}{RT}\left(1 - \frac{T}{T_{\mathrm{ref}}}\right)\right] \tag{6}$$

where $\xi = RT/H_0$ is a uptake coefficient, based on Henry's law [11], accounting for the difference in the oxygen concentration in the gas and ionomer phase. Moreover, the exchange current density is corrected for its temperature dependence and active sites being blocked.

The electrochemical reactions in the CL introduce sink and source terms in the continuity equation. Since water is produced it is a mass source and because oxygen is consumed it is a mass sink. Each term depends on the current density drawn from the PEMFC and the number of electrons involved in the consumption or formation of a given species:

$$S_{g_{\mathrm{O}_2}} = -\frac{jM_{\mathrm{O}_2}}{4F} \quad \vee \quad S_{l_{\mathrm{H_2O}}} = \frac{jM_{\mathrm{H_2O}}}{2F} \tag{7}$$

In a porous medium the momentum source term can be formulated in terms of a constant, linear, and quadratic resistance, also known as the generalized Darcy's law or Darcy-Forchheimer equation. By replacing the liquid pressure gradient in the momentum equation by the sum of the gas and capillary pressure gradient, the constant term appears in the liquid phase. Effectively, the capillary pressure gradient imposes a liquid bulk movement in the direction of decreasing capillary pressure.

$$\mathbf{S}_{g,\mathrm{mom}} = -\frac{\mu}{k_{\mathrm{rel}}}\bar{K}^{-1}\mathbf{U}_g - \frac{\varepsilon\rho}{k_{\mathrm{rel}}}\bar{\beta}|\mathbf{U}_g|\mathbf{U}_g - \nabla p_g \tag{8}$$

$$\mathbf{S}_{l,\mathrm{mom}} = \nabla p_{\mathrm{cap}} - \frac{\mu}{k_{\mathrm{rel}}}\bar{K}^{-1}\mathbf{U}_l - \frac{\varepsilon\rho}{k_{\mathrm{rel}}}\bar{\beta}|\mathbf{U}_l|\mathbf{U}_l - \nabla p_g \tag{9}$$

In general the relative permeability depends on pore structure, wettability, capillary forces, and saturation history [12], however it is normally modeled as being dependent only upon liquid phase saturation:

$$k_{\mathrm{rel},g} = (1-s)^q \quad \vee \quad k_{\mathrm{rel},l} = s^q \tag{10}$$

In the literature different values of q have been employed. However, a general consensus has been established on a cubic dependence; thus implying a strong interaction with local saturation [2,4,13,14]. This assumption was further experimentally verified by Nam and Kaviany [15].

Water vapor condenses either on a pre-existing liquid layer or on a hydrophilic surface [15]. In the channel, the wall surface is typically hydrophobic; hence water only condenses on pre-existing water droplets. By contrast, inside porous media, a fraction of the surface is hydrophilic, and hence can accommodate water droplets. In contrary to condensation, evaporation can only occur from an pre-existing liquid surface area. In order to model the phase change rate one needs to determine the specific liquid-gas interfacial area of mass transfer A_{lg}. In a free stream it is a common simplification is to assume that the liquid phase exist as spherical droplets of fixed and equal size. However, inside porous media it is reasonable to assume that the specific interfacial area depends on the pore surface area [15]. Furthermore, since water only evaporates from a pre-existing liquid surface and condensation depends on the volume fraction of gas, the following type correction is used to distinguish between condensation and evaporation:

$$A_{lg} = \begin{cases} \varepsilon\,(1-s)\Gamma_s A_{\mathrm{pore}} & p_{\mathrm{H_2O}} > p_{\mathrm{sat}} \\ \varepsilon\, s\Gamma_s A_{\mathrm{pore}} & p_{\mathrm{H_2O}} < p_{\mathrm{sat}} \end{cases} \tag{11}$$

where A_{pore} is specific pore surface area, and Γ_s is the surface accommodation coefficient. The phase change rate is expressed as the relative deviation from the thermodynamic equilibrium pressure at the interface, equivalent to a mass transfer limitation [12,16]:

$$\dot{m}_{\alpha\beta} = k_{xm}A_{lg}MW_{\mathrm{H_2O}}\frac{p_{\mathrm{H_2O}} - p_{\mathrm{H_2O,sat}}(T)}{RT} \tag{12}$$

where k_{xm} is the convective mass transfer coefficient (m s^{-1}). Alternatively a thermodynamic phase equilibrium is often assumed at the interface [17]. Such an approach assumes a high convective mass transfer coefficient, as shown by [18].

In porous media, the phase change rate can be calculated based on kinetic theory and the assumption of ideal gas behavior. However, the diffusion process needs to be corrected due to the presence of other species by accounting for intermolecular collisions. Furthermore, the ability of the droplet to absorb water molecules needs to be accounted for [15]:

$$k_{xm} = \Gamma_u \bar{u}_m = \Gamma_u\sqrt{\frac{8R_gT}{\pi MW}} \tag{13}$$

where Γ_u is the uptake coefficient, which accounts for the presence of noncondensable species at the gas-liquid interface, and α_m is the mass accommodation coefficient (–).

Due to the electrochemical reaction, reversible and irreversible heat is generated. It has been experimentally determined that the heat produced due to entropy generation is inherently found at the cathode only. Furthermore, due to evaporation/condensation latent heat is either removed or added. Based on these two mechanisms the following heat source can be formulated [19]:

$$S_T\left(\frac{T\Delta s_r}{nF} + \eta_{\mathrm{act}}\right)j_{\mathrm{O_2}} + \dot{m}_{\alpha\beta}h_{lg} \tag{14}$$

2.5 Properties. The saturation pressure has a strong nonlinear dependence on temperature. To improve numerical robustness a curve fit of this equation is implemented [4]:

$$p_{\mathrm{sat}}(T) = 0.239T^3 - 220T^2 + 6.81\times10^4T - 7.06\times10^6 \tag{15}$$

which is valid for $T \in [(313, 373)]$ K. Furthermore, the saturation pressure equilibrium inside the porous medium is corrected for capillary condensation by the Kelvin equation [20]:

$$p_{\mathrm{sat,corr}}(T) = p_{\mathrm{sat}}(T)\exp\left(-\frac{MW_{\mathrm{H_2O}}4\sigma\cos\theta}{\rho_{\mathrm{H_2O},l}\;RTD_c}\right) \tag{16}$$

It is convenient to describe the capillary pressure in terms of the Leverett's function, hereby making it a function of fluid properties, geometry, and water saturation. This approach was first proposed in [21] and since utilized by several groups [1,2,4,14,15,22]:

$$p_{\mathrm{cap}} = \sigma\cos\theta\left(\frac{\varepsilon}{K}\right)^{\frac{1}{2}}J(S) \tag{17}$$

$$J(s) = \begin{cases} 1.417(1-S) - 2.12(1-S)^2 + 1.263(1-S)^3 & \theta < 90 \\ 1.417S - 2.12S^2 + 1.263S^3 & \theta > 90 \end{cases}$$

where σ denotes surface tension, θ is the contact angle, ε is the porosity, K is the effective permeability, S is the effective volume fraction, and $J(S)$ is the Leverett function. It should be noted that the validity of the Leverett J function is highly discussed as pointed out in [5] among others. This discussion was further substantiated in [11]. In their paper they compared different capillary pressure models and showed that liquid water distribution is highly dependent upon the model used.

The effective saturation is a function used to account for the irreducible saturation content of a porous medium, and it is a function of total saturation and irreducible saturation [15]:

$$S = \frac{s - s_{\mathrm{irr}}}{1 - s_{\mathrm{irr}}} \tag{18}$$

where s is liquid water saturation and s_{irr} is the irreducible saturation. This approach is widely adopted and has been utilized by [4,14,15] among others.

Kinematic diffusivity is a mechanism of transport essentially caused by molecular collisions facilitating movement of species in the direction of decreasing concentration. The diffusivity of a certain species in a mixture of several species can be estimated using [23]

$$D_{A\alpha}(T_0, p_0) = (1 - x_A)\left(\sum_{i\neq A}^{n}\frac{x_i}{D_{Ai}}\right)^{-1} \tag{19}$$

where $D_{A\alpha}$ is the diffusion coefficient of component A in phase α. Furthermore, kinematic diffusivity is temperature and pressure

dependent. This is typically accounted for by the following equation [3]:

$$D_{A\alpha}(T,p) = D_{A\alpha}(T_0,p_0)\frac{p_0}{p}\left(\frac{T}{T_0}\right)^{\frac{3}{2}} \tag{20}$$

In the porous layers, such properties as tortuosity, porosity, and liquid water saturation are accounted for as follows:

$$D_{A\alpha}^{\text{eff}} = \frac{1}{\tau}(1-s)^p D_{A\alpha}(T,p) \tag{21}$$

where τ denotes tortuosity and s is the liquid phase saturation. Equation (21) utilizes that Eq. (4) already accounts for porosity and further accounts for a higher dependence on liquid water saturation. The exponent p was determined experimentally to be unity, in order to end up with an overall second order dependence on water saturation in Eq. (4) [15]. In essence the saturation term accounts for the decrease in the diffusion area due to liquid water.

Inside the CL diffusion is no longer controlled merely by molecular collisions. The pore diameter in the CL is so small that it can be less than the molecular mean free path of the gas particles. In this range particle-wall collisions become important and need to be accounted for. [3,24] This phenomenon is called Knudsen diffusion and can be estimated via the dimensionless Knudsen number, which is the ratio between molecular mean free path and the characteristic pore diameter. The Knudsen transition scheme is defined as the range $0.01 < \text{Kn} < 1$. Knudsen diffusivity can be calculated from collision theory as follows:

$$D_{A\alpha}^{K} = \frac{D_{\text{pore}}}{3}\sqrt{\frac{8RT}{\pi MW_g}} \tag{22}$$

The combined diffusivity due to particle-particle and particle-wall collisions can be expressed as a sum diffusion resistances:

$$D_{A\alpha} = \frac{D_{A\alpha}^{\text{eff}} D_{A\alpha}^{K}}{D_{A\alpha}^{\text{eff}} + D_{A\alpha}^{K}} \tag{23}$$

2.6 Inhomogeneous Properties. In order to model and investigate the effect of inhomogeneous GDL material properties, information is needed on the dependence of such properties as porosity, tortuosity and permeability, on applied clamping pressure, and position. In essence these properties can all be correlated to the volume/thickness change of the GDL [8,25]. Moreover, the change in thickness can be estimated as a function of strain and channel intrusion. When a pressure is applied to the under-the-land area, the encountered stress is distributed over both the channel area and under-the-land area. Hence the calculated force should be corrected for the effective compression area. This can be done by introducing an average strain in the through-plane direction, based on the average thickness:

$$\varepsilon_s = \frac{t_0 - \bar{t}}{t_0} = 1 - \frac{1}{t_0 w_{\text{tot}}}\int_0^{w_{\text{tot}}} t dx \tag{24}$$

If Eq. (24) is rewritten in terms of the maximum intrusion, the following function of the GDL thickness can be derived by assuming a parabolic intrusion:

$$t_{\text{int}}(x) = \frac{2t_{\text{int,max}}}{x_{\text{max}}}x - \frac{2t_{\text{int,max}}}{x_{\text{max}}^2}x^2 \tag{25}$$

$$t(x) = \begin{cases} t_0(1-\varepsilon_s) - \dfrac{2}{3}t_{\text{int,max}}\dfrac{w_{\text{ch}}}{w_{\text{ul}}+w_{\text{ch}}} & x \le w_{\text{ul}} \\ t_0(1-\varepsilon_s) + t_{\text{int}}(x) - \dfrac{2}{3}t_{\text{int,max}}\dfrac{w_{\text{ch}}}{w_{\text{ul}}+w_{\text{ch}}} & x > w_{\text{ul}} \end{cases} \tag{26}$$

It is important to note that the true intrusion shape depends on the structural properties of the GDL. Therefore, for simplification a parabolic dependence is assumed. In the literature quite different dependencies have been reported. A logarithmic dependence was reported by [7] and a third-order polynomial relation by [8]. A compression normalized comparison with [7,8] showed good agreement.

It should be noted that this model does not take the through-plane porosity variation fully into account. As was shown by [26] the porosity of a typical GDL decreases towards the GDL core, with different shapes depending on the GDL.

2.6.1 Strain and Intrusion. In the paper by Lai et al. [27] the authors measured the intrusion into a 1 mm wide channel and compressive strain in the through-plane direction of a carbon paper based GDL, and compared their results to a finite element model. It was underlined that the lower the shear and bending stiffness the higher the intrusion. The following equations where fitted to these measurements of the strain and intrusion as function of compression, respectively:

$$\varepsilon_s = 4.979\times10^{-3}p + 3.522\times10^{-3}p^2 + 1.169\times10^{-1}p^{\frac{1}{2}} \tag{27}$$

$$t_{\text{int}} = 1.352\times10^{-5}p - 1.008\times10^{-6}p^2 + 2.942\times10^{-5}p^{\frac{1}{2}} \tag{28}$$

where p is the compression pressure in MPa and t_{int} is the intrusion in meters.

2.6.2 Porosity. When assuming that deformation due to compression can only occur in the through-plane direction since movement in the in-plane direction is obstructed, and further assuming that the change in porosity only occurs due to a reduction in pore volume, the porosity becomes a function of thickness change:

$$\varepsilon = 1 - \frac{t_0}{t(x)}(1-\varepsilon_0) \tag{29}$$

A similar approach of relating the thickness change to a porosity change was taken in [7,8,25]. A qualitative comparison between our modeled compression dependent porosity and the one measured as a function of compression by [28] revealed similar dependence.

2.6.3 Tortuosity and Permeability. The tortuosity and viscous permeability of a fibrous porous medium can be estimated via the following empirical correlations as a function of porosity [29]:

$$\tau = \left(\frac{1-\varepsilon_p}{\varepsilon-\varepsilon_p}\right)^{\alpha} \tag{30}$$

$$K = \frac{\varepsilon}{8(\ln\varepsilon)^2(1-\varepsilon_p)^{\alpha}}\frac{(\varepsilon-\varepsilon_p)^{\alpha+2}r_f^2}{\left[(\alpha+1)\varepsilon-\varepsilon_p\right]^2} \tag{31}$$

where ε_p is the percolation threshold porosity, which for two-dimensional fibrous structures is 0.11, r_f is the carbon fiber radius and α is a directional dependent parameter, which in the through-plane and in-plane direction is 0.521 and 0.785, respectively. Equations (30) and (31) were originally fitted to the resulting diffusivity and permeability of Monte Carlo simulations of modeled randomly oriented fibrous porous media. Similarly to Ref. [25] it is assumed that the percolation threshold and the other structural constants do not change with compression.

Furthermore, based on the tortuosity and viscous permeability the inertial permeability can be estimated using the following equation [30]:

$$\beta = 2.88\times10^{-6}\frac{\tau}{\varepsilon K} \tag{32}$$

Table 1 Model properties

Parameter	Symbol	Expression
Latent heat of evaporation/condensation (J/mol)	h_{lg}	$57{,}555.684 - 45.36T$
Henry's constant (Pa/m^3 mol)	H_0	2.0×10^4
Entropy change (J/mol K)	Δs	149.14
Catalyst activation energy (kJ/mol)	$E_{\text{act,cat}}$	66.0
Air stoichiometry	λ_{O_2}	10
Inlet RH (%)	RH	75
Porosity (CL, MPL and GDL) (–)	ε	0.12, 0.4, 0.75
Permeability (CL) (m^2)	–	2.5×10^{-15}
GDL conductivity (W/m K)	k	1.3
Compression (MPa)	p_{comp}	3.0
Thickness (CL, MPL, and GDL) (μm)	t	348, 20, 20
Uptake coefficient (–)	Γ_u	0.06
Surface accommodation coefficient (–)	Γ_s	0.01
Specific surface area (1/m)	a	1.0×10^6
Contact angle of CL, GDL, and MPL (deg)	θ	110
Irreducible saturation	s_{irr}	0.01
Inlet nitrogen conc.	$C_{N_2,\text{in}}$	$0.79\,(P - RHp_{\text{sat}})\,/\,RT$
Inlet oxygen conc.	$C_{O_2,\text{in}}$	$0.21\,(P - RHp_{\text{sat}})\,/\,RT$
Inlet water vapor conc.	$C_{C_{H_2O},\text{in}}$	RHp_{sat}/RT

Table 2 Selected simulation results

Parameter	Homogeneous	Inhomogeneous
Avg. porosity in GDL (–)	0.75	0.67
Avg. current density (A/cm^2)	0.761	0.738

2.7 Boundary and Initial Conditions. The PEMFC model uses mass flow inlet and pressure outlet. The inlet liquid phase saturation is zero and the inlet temperature is 314 K. The inlet mass flow of gas and its mass fractions of water and oxygen are calculated as follows:

$$\dot{m}_{\text{gas}} = \frac{\rho_{\text{gas}} \lambda_{O_2} \int_V j dV}{4FCo_2} \tag{33}$$

$$Y_i = \frac{C_i MW_i}{\Sigma_{i=1}^{N} C_i MW_i} \tag{34}$$

At the boundary facing the middle of the channel and facing the middle of the bipolar plate symmetry planes are specified. At the remaining boundaries a wall boundary with a no-slip condition is specified.

3 Results

In this section the specified material properties, overall solver settings, and simulation results are shown. The specified material properties are shown in Table 1. The solution was obtained by running the CFX 13 solver with a higher order advection scheme and a coupled velocity, pressure, and volume fraction solver. Furthermore, in order to obtain convergence a false time step relaxation and source term linearization strategy was used.

Under the assumption that the PEMFC is compressed by 3.0 MPa a new GDL thickness under the land of 131.8 μm is obtained. This compression corresponds to a thickness reduction of $\sim$100 μm. To ensure that the liquid phase reaches the GDL-channel interface, and does not become evaporated before reaching the interface, a relative low cooling temperature of 313 K is specified. Furthermore, at the specified overvoltage loss of 0.72 V, the PEMFCs produced the tabulated values in Table 2. These load conditions lead to the liquid water volume fraction, oxygen molar fraction, and phase change rate distribution shown in Figs. 2–4, respectively.

4 Discussion

From the simulation results shown in Table 2, it can be deduced that inhomogeneous compression decreases the reaction rate in the CL of the cathode. The performance of the PEMFC decreased by 3%. Since both simulation cases are operated under the same prescribed conditions, the decrease in reaction rate must be caused by the inhomogeneous compression of the GDL.

Inherently, oxygen transport decreases when the porosity and permeability decreases, and tortuosity increases. Consequently, a decrease in oxygen concentration in the CL is observed when

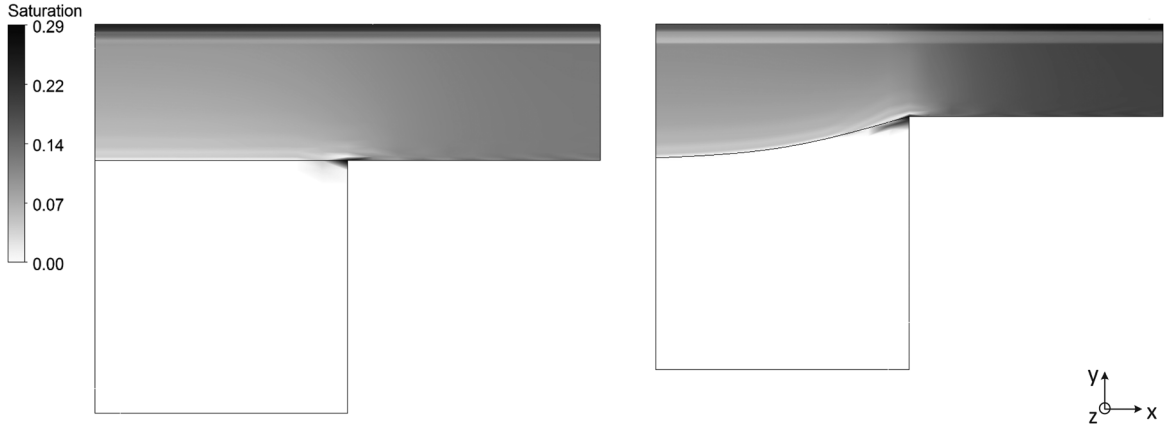

Fig. 2 Liquid volume fraction/saturation distribution without and with compression

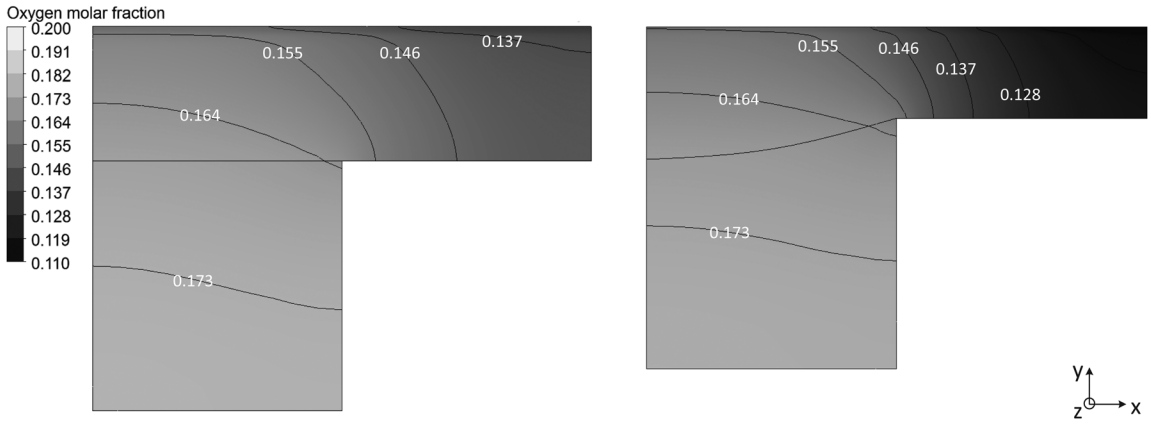

Fig. 3 Oxygen molar fraction distribution without and with compression

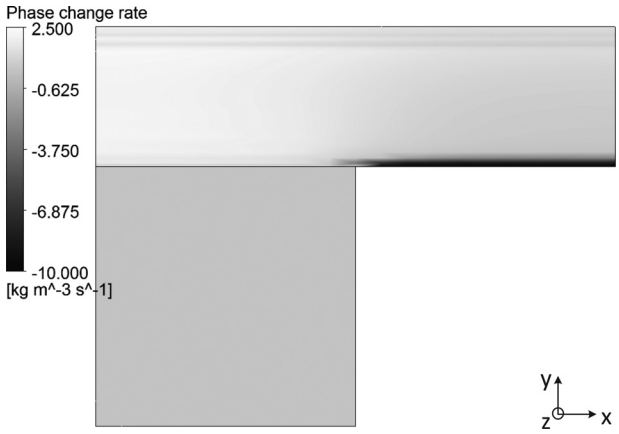

Fig. 4 Phase change rate without compression

comparing the distributions in Fig. 3. Moreover, the oxygen transport is further obstructed by an increase in the liquid water volume fraction in the GDL under the land, as seen when comparing the distributions in Fig. 2. However, this increase in liquid volume fraction is small, and hence has a minor impact.

In both cases the lowest oxygen concentration is found under the land. Equivalently, the lowest current density is found here. This observation is in contradistinction to the one made by Nitta et al. [8]. Their study showed that the highest current density is seen under the land. One reason for this observed difference might be the importance of accounting for two-phase flow and nonequilibrium phase change.

In Fig. 4 two distinct phase change fronts are visible. Evaporation at the CL and condensation under-the-land area. Interestingly, the largest evaporation rate is found mid under the channel in the CL. Hence, not accounting for evaporation could lead to a much higher liquid phase volume fraction prediction and hence a much higher active site blocking. Furthermore, the predicted condensation rate is highest under-the-land area near the bipolar plate due to cooling. Again, not accounting for condensation would underpredict the liquid phase volume fraction and pore blocking in the GDL under-the-land area.

When further analyzing the liquid volume fraction distribution, two clear saturation jumps are observed in both cases at the MPL-CL and GDL-MPL interface. This jump phenomenon occurs since the capillary pressure has to be continuous. In order to satisfy this pressure condition a jump condition has to arise in the liquid volume fraction profile, when a change in material properties occurs. From the channel-GDL interface towards the GDL-MPL interface an increase in liquid volume fraction is observed under the channel. Whereas it is fairly constant under the land. However, from the GDL-MPL interface toward MPL-CL interface an increase in liquid volume fraction is seen under both the channel and land. Furthermore, in the case of inhomogeneous compression the largest liquid volume fraction is found in the CL under the channel, as opposed to the case without compression, where an even distribution is seen. As the GDL becomes more and more compressed, the oxygen transport rate decrease under-the-land area. Consequently, the liquid water production and liquid volume fraction decreases in CL under-the-land area. However, the liquid volume fraction is not only dependent on the production rate, but also the transport rate, which in turn is dependent on the capillary pressure gradient, Darcy resistance, phase change kinetics, and operation conditions.

Comparing the liquid saturation profile in the case without compression with the modeling study by Basu et al. [17] reveals that our model predicts a higher liquid saturation in the CL under the channel. This difference is partly influenced by fact that our model does not account for water transport through the membrane. Moreover, there is a clear difference in the capillary pressure distribution and phase change kinetics. The model by Basu et al. [17] does not account for a MPL nor does it appear to be able to account for the liquid saturation jump condition between the individual layers. Hence, it may overpredict the liquid water transport rate under the channel, by not properly accounting for the liquid water hold up. It can be shown, by increasing the permeability of the CL and MPL, that the liquid volume fraction profile can be altered such that less water is observed under the channel than under the land in CL. Furthermore, their model assumes thermodynamic phase equilibrium and hence inherently assumes very fast phase change kinetics. Consequently, by similarly increasing our models phase change coefficient more liquid would become evaporated under the channel in the CL layer, lowering the liquid volume fraction.

In future work it would be beneficial to do a detailed verification of the porosity, permeability, and tortousity distributions as a function of clamping pressure. Such verification could be done by comparing with measurements found in the literature [7,28]. Alternatively, a FEM study of the GDL intrusion and porosity distribution as a function of clamping pressure could be done, similarly as in [9].

Acknowledgment

This work was partially supported by the Danish Energy program, 2008-1-10076, Aalborg University, and the HyFC Research School.

Nomenclature

A = area (m^2)
a = specific area (m^2/m^3)
C = molar fraction (–)
D = diffusivity (m^2/s)

F = Faradays constant (C/mol)
K = viscous permeability (m^2)
H = static enthalpy (J)
h = specific enthalpy (J/kg)
l = length (m)
$\dot{m}$ = mass flow (kg/s)
P = pressure (Pa)
p = partial pressure (Pa)
S = source term
T = temperature (K)
t = thickness (m)
U = velocity vector (m/s)
w = width (m)
X = mole fraction
Y = mass fraction
β = inertial permeability (1/m)
ε = porosity or strain (m/m)
ρ = density (kg/m^3)
τ = tortousity
Γ = accommodation coefficient
α = phase
ch = channel
eff = effective
g = gas phase
irr = irreducible
l = liquid phase
s = strain
ul = under land

References

[1] Berning, T., and Djilali, N., 2003, "A 3D, Multiphase, Multicomponent Model of the Cathode and Anode of a PEM Fuel Cell," J. Electrochem. Soc., **150**, pp. A1589–A1598.
[2] Mazunder, S., and Cole, J. V., 2003, "Rigorous 3-D Mathematical Modelling if PEM Fuel Cells," J. Electrochem. Soc., **150**, pp. A1510–A1517.
[3] Wang, C., 2004, "Fundamental Models for Fuel Cell Engineering," Chem. Rev., **104**, pp. 4727–4766.
[4] Berning, T., Odgaard, M., and Kr, S. K., 2009, "A Computational Analysis of Multiphase Flow Through PEMFC Cathode Porous Media Using the Multifluid Approach," J. Electrochem. Soc., **156**, pp. B1301–B1311.
[5] Gurau, V., Thomas A., Zawodzinski, J., and J. Adin Mann, J., 2008, "Two-Phase Transport in PEM Fuel Cell Cathodes," ASME J. Fuel Cell Sci. Technol., **5**(2), p. 021009.
[6] Cindrella, L., Kannan, A., Lin, J., Saminathan, K., Ho, Y., Lin, C., and Wertz, J., 2009. "Gas Diffusion Layer for Proton Exchange Membrane Fuel Cells—A Review," J. Power Sources, **194**(1), pp. 146–160.
[7] Hottinen, T., Himanen, O., Karvonen, S., and Nitta, I., 2007, "Inhomogeneous Compression of PEMFC Gas Diffusion Layer Part II. Modeling the Effect," J. Power Sources, **171**, pp. 113–121.
[8] Nitta, I., Karvonen, S., Himanen, O., and Mikkola, M., 2008, "Modelling the Effect of Inhomogeneous Compression of GDL on Local Transport Phenomena in a PEM Fuel Cell," Fuel Cells, **6**, pp. 410–421.
[9] Zhou, P., and Wu, C., 2007, "Numerical Study on the Compression Effect of Gas Diffusion Layer on PEMFC Performance," J. Power Sources, **170**(1), pp. 93–100.
[10] Spiegel, C., 2008, *PEM Fuel Cell Modeling and Simulation Using Matlab*, Academic, New York.
[11] Wu, H., Li, X., and Berg, P., 2009, "On the Modeling of Water Transport in Polymer Electrolyte Membrane Fuel Cells," Electrochim. Acta, **54**(27), pp. 6913–6927.
[12] Dong, M., and Dullien, F. A. L., 2006, *Multiphase Flow Handbook*, Taylor & Francis, London.
[13] Weber, A. Z., and Newman, J., 2004. "Modeling Transport in Polymer-Electrolyte Fuel Cells," Chem. Rev., **104**(10), pp. 4679–4726.
[14] Wang, Y., Basu, S., and Wang, C.-Y., 2008, "Modeling Two-Phase Flow in PEM Fuel Cell Channels," J. Power Sources, **179**(2), pp. 603–617.
[15] Nam, J. H., and Kaviany, M., 2003, "Effective Diffusivity and Water-Saturation Distribution in Single- and Two-Layer PEMFC Diffusion Medium," Int. J. Heat Mass Transfer, **46**(24), pp. 4595–4611.
[16] Berning, T., Odgaard, M., and Kær, S. K., 2010, "A Study of Multi-Phase Flow Through the Cathode Side of an Interdigitated Flow Field Using a Multi-Fluid Model," J. Power Sources, **195**(15), pp. 4842–4852.
[17] Basu, S., Wang, C.-Y., and Chen, K. S., 2009, "Phase Change in a Polymer Electrolyte Fuel Cell," J. Electrochem. Soc., **156**(6), pp. B748–B756.
[18] Meng, H., 2007, "Numerical Investigation of Transient Responses of a PEM Fuel Cell Using a Two-Phase Non-Isothermal Mixed-Domain Model," J. Power Sources, **171**(2), pp. 738–746.
[19] Lampinen, M. J., and Fomino, M., 1993, "Analysis of Free Energy and Entropy Changes for Half-Cell Reactions," J. Electrochem. Soc., **140**, pp. 3537–3546.
[20] Eikerling, M., 2006, "Water Management in Cathode Catalyst Layers of PEM Fuel Cells—A Structure-Based Model," J. Electrochem. Soc., **153**, pp. E58–E70.
[21] Udell, K. S., 1985, "Heat-Transfer in Porous-Media Considering Phase-Change and Capillarity—The Heat Pipe Effect," Int. J. Heat Mass Transfer, **28**, pp. 485–495.
[22] Pasaogullari, U., and Wang, C. Y., 2004, "Liquid Water Transport in Gas Diffusion Layer of Polymer Electrolyte Fuel Cells," J. Electrochem. Soc., **151**(3), pp. A399–A406.
[23] Bird, R. B., Stewart, W. E., and Lightfoot, E. N., 2007, *Transport Phenomena*, 2nd ed., John Wiley, New York.
[24] Gurau, W., and Mann, J. A. J., 2009, "A Critical Overview of Computational Fluid Dynamics Multiphase Models for Proton Exchange Membrane Fuel Cells," SIAM J. Appl. Math., **70**, pp. 410–454.
[25] Gostick, J. T., Fowler, M. W., Pritzker, M. D., Ioannidis, M. A., and Behra, L. M., 2006, "In-Plane and Through-Plane Gas Permeability of Carbon Fiber Electrode Backing Layers," J. Power Sources, **162**(1), pp. 228–238.
[26] Fishman, Z., and Bazylak, A., 2011, "Heterogeneous Through-Plane Distributions of Tortuosity, Effective Diffusivity, and Permeability for PEMFC GDLs," J. Electrochem. Soc., **158**(2), pp. B247–B252.
[27] Lai, Y.-H., Pinkhas, A. R., Ji, C., and Kumar, V., 2008, "Channel Intrusion of Gas Diffusion Media and the Effect on Fuel Cell Performance," J. Power Sources, **184**, pp. 120–128.
[28] Chang, W., Hwang, J., Weng, F., and Chan, S., 2007, "Effect of Clamping Pressure on the Performance of a PEM Fuel Cell," J. Power Sources, **166(1)**, pp. 149–154.
[29] Tomadakis, M. M., and Robertson, T. J., 2005, "Viscous Permeability of Random Fiber Structures: Comparison of Electrical and Diffusional Estimates With Experimental and Analytical Results," J. Composite Mater., **39**(2), pp. 163–188.
[30] Liu, X., Civan, F., and Evans, R. D., 1995, "Correlation of the Non-Darcy Flow Coefficient," J. Can. Pet. Technol., **34**, pp. 50–54.